ACSNANO

www.acsnano.org

ARTICLE

Tunable Electromechanical Nanopore Trap Reveals Populations of Peripheral Membrane Protein Binding Conformations

David P. Hoogerheide,* Tatiana K. Rostovtseva, Daniel Jacobs, Philip A. Gurnev, and Sergey M. Bezrukov

Cite This: *ACS Nano* 2021, 15, 989−1001

Read Online

ACCESS | Metrics & More | Article Recommendations

ABSTRACT: We demonstrate that a naturally occurring nanopore, the voltage-dependent anion channel (VDAC) of the mitochondrion, can be used to electromechanically trap and interrogate proteins bound to a lipid surface at the single-molecule level. Electromechanically probing α-synuclein (αSyn), an intrinsically disordered neuronal protein intimately associated with Parkinson's pathology, reveals wide variation in the time required for individual proteins to unbind from the same membrane surface. The observed distributions of unbinding times span up to 3 orders of magnitude and depend strongly on the lipid composition of the membrane; surprisingly, lipid membranes to which αSyn binds weakly are most likely to contain subpopulations in which electromechanically driven unbinding is very slow. We conclude that unbinding of αSyn from the membrane surface depends not only on membrane binding affinity but also on the conformation adopted by an individual αSyn molecule on the membrane surface.

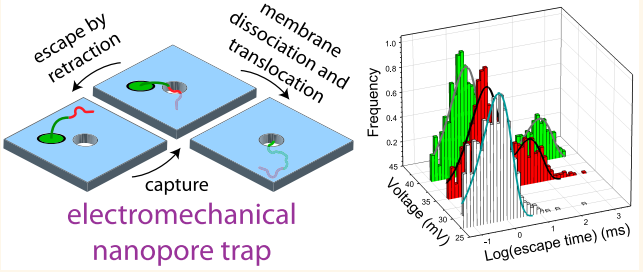

KEYWORDS: *voltage-dependent anion channel, α-synuclein, intrinsically disordered proteins, protein−lipid interaction, single-molecule measurement, peripheral membrane proteins, energy landscape*

The capture and analysis of charged biomolecules by nanopores has revolutionized single-molecule sensing. A nanopore is a small hole in a thin membrane separating two electrically isolated reservoirs filled with electrolyte solution. In a conventional nanopore sensing experiment, a transmembrane potential is applied across the membrane, creating a small ionic current through the nanopore. Often, the transmembrane potential is also responsible for attracting, capturing, and driving the analyte through the interior of the nanopore. Modulations in the ionic current in the presence of large analyte biomolecules such as polynucleic acids or proteins contain information about their structure and dynamics. The membrane can be constructed from either solid-state materials or lipid membranes; in the latter case, the nanopore is often a naturally occurring or engineered ion channel. While the primary application of nanopores remains the rapid sequencing of polynucleic acids, proteins and their vast array of known properties and interactions are of continued interest. In this context, nanopores have been used for low-resolution analysis of conformation, shape, and tumbling dynamics,[1] analysis of post-translational modifications and other single-residue alterations,[2−4] protein fingerprinting, and protein−ligand interactions.[5] Active development is underway to apply nanopore-based sensing to protein sequencing and proteomic analysis.[6−8]

Biological nanopores are embedded in lipid membranes and are thus in close proximity to other membrane-associated proteins in, or transiently interacting with, the membranes. As a result of their strategic location *in vivo* at the boundaries of cells and their compartments, membrane-associated proteins play an outsized role in how cells process and respond to their environment. While membrane proteins are estimated to constitute only about 20% of the human proteome,[9] they represent about 70% of modern drug targets.[10] Their confinement to the crowded two-dimensional membrane surface, however, limits the number of copies of these proteins found in

Received: September 11, 2020
Accepted: December 16, 2020
Published: December 28, 2020

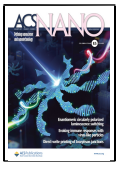

https://dx.doi.org/10.1021/acsnano.0c07672
ACS Nano 2021, 15, 989−1001

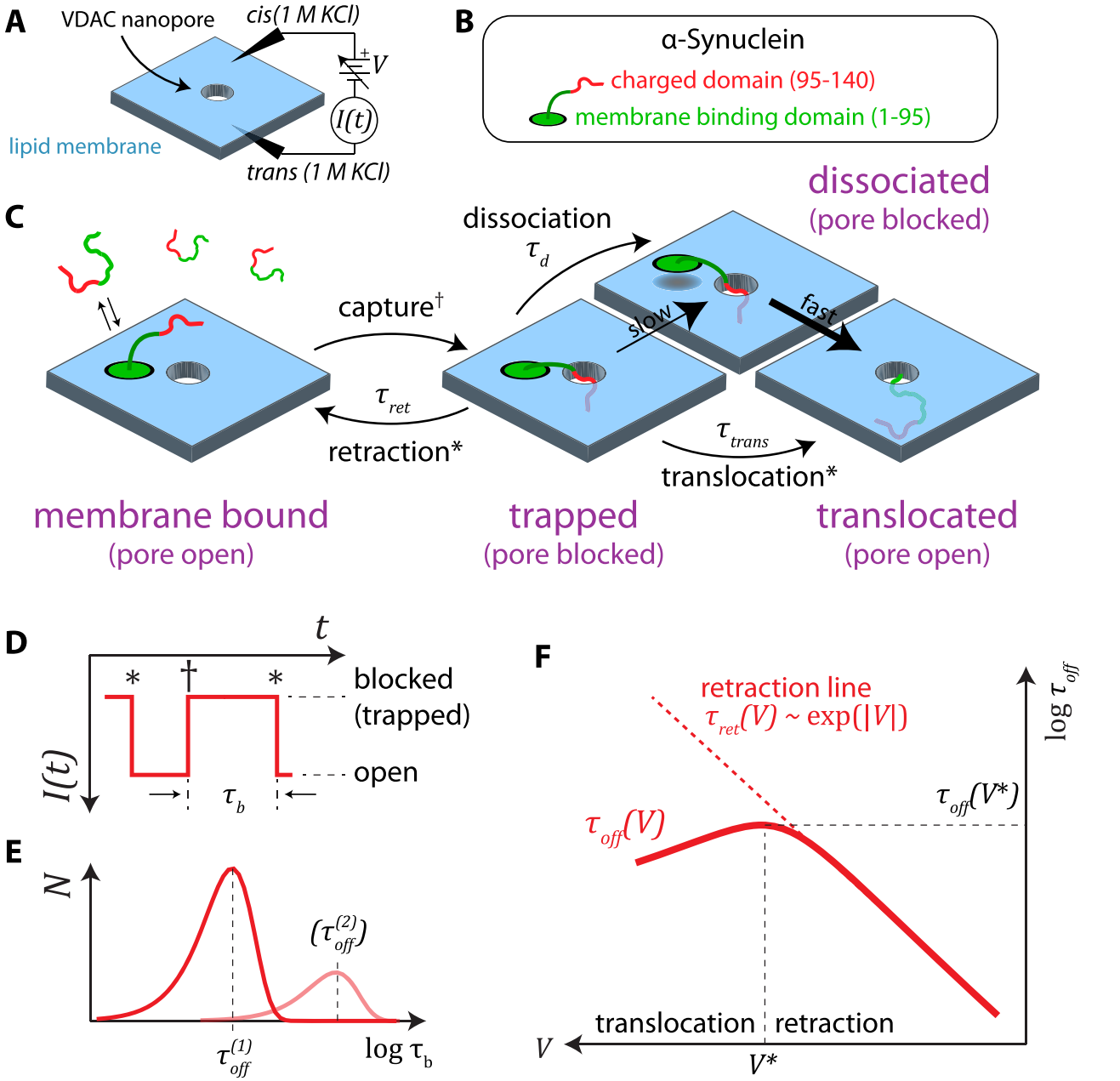

Figure 1. Schematic of the electromechanical nanopore trapping process. (A) VDAC nanopore is reconstituted into a lipid membrane and subjected to a transmembrane potential V, setting up an ionic current $I(t)$ through the nanopore. (B) Peripheral membrane protein α-synuclein (αSyn) has a nonuniform charge density, with a two-region structure comprising a negatively charged domain and a net neutral membrane binding domain. (C) Charged domain of αSyn is captured by the (negative) transmembrane potential and remains trapped by the opposing action of the electrostatic and mechanical membrane anchoring forces. Eventually it escapes either by retraction from, or translocation through, the nanopore. Processes corresponding to escape and capture are denoted by * and †, respectively. (D) $I(t)$ directly reports on whether an αSyn molecule is trapped in the nanopore. Abrupt changes in the ionic current corresponding to escape and capture processes are marked with the same symbols as in (C). The duration of a single blockage event is τ_b. (E) Distributions of τ_b are plotted on a logarithmic time axis. The curves shown are single-exponential functions with characteristic escape times τ_{off}; more than one can be present and are revealed by interrogating individual molecules. (F) V dependence of τ_{off} reveals the underlying dynamics. τ_{off} is primarily determined by the exponential dependence of the average retraction time τ_{ret} (dashed line) up to a transition voltage V^*, above which translocation dominates.

cells and makes them difficult to study by conventional solution-based biochemical and biophysical techniques in which their natural membrane environment is not present.

Peripheral membrane proteins are a subclass of membrane-associated proteins that are only transiently bound to the lipid surface. This property allows these molecules to take advantage both of the enhancement of interaction rate with other membrane proteins when localized on the membrane surface and, when unbound, of a higher rate of transport through solution. The multicomponent nature of lipid-mediated protein−protein interactions, the transience of the protein association with lipid membranes, and the differences in their structural and biochemical properties in their membrane-bound and solvated states[11−13] all complicate the study of peripheral membrane proteins. Dynamical biophysical techniques that allow probing the proteins, or their effects on lipid membranes,

https://dx.doi.org/10.1021/acsnano.0c07672
ACS Nano 2021, 15, 989−1001

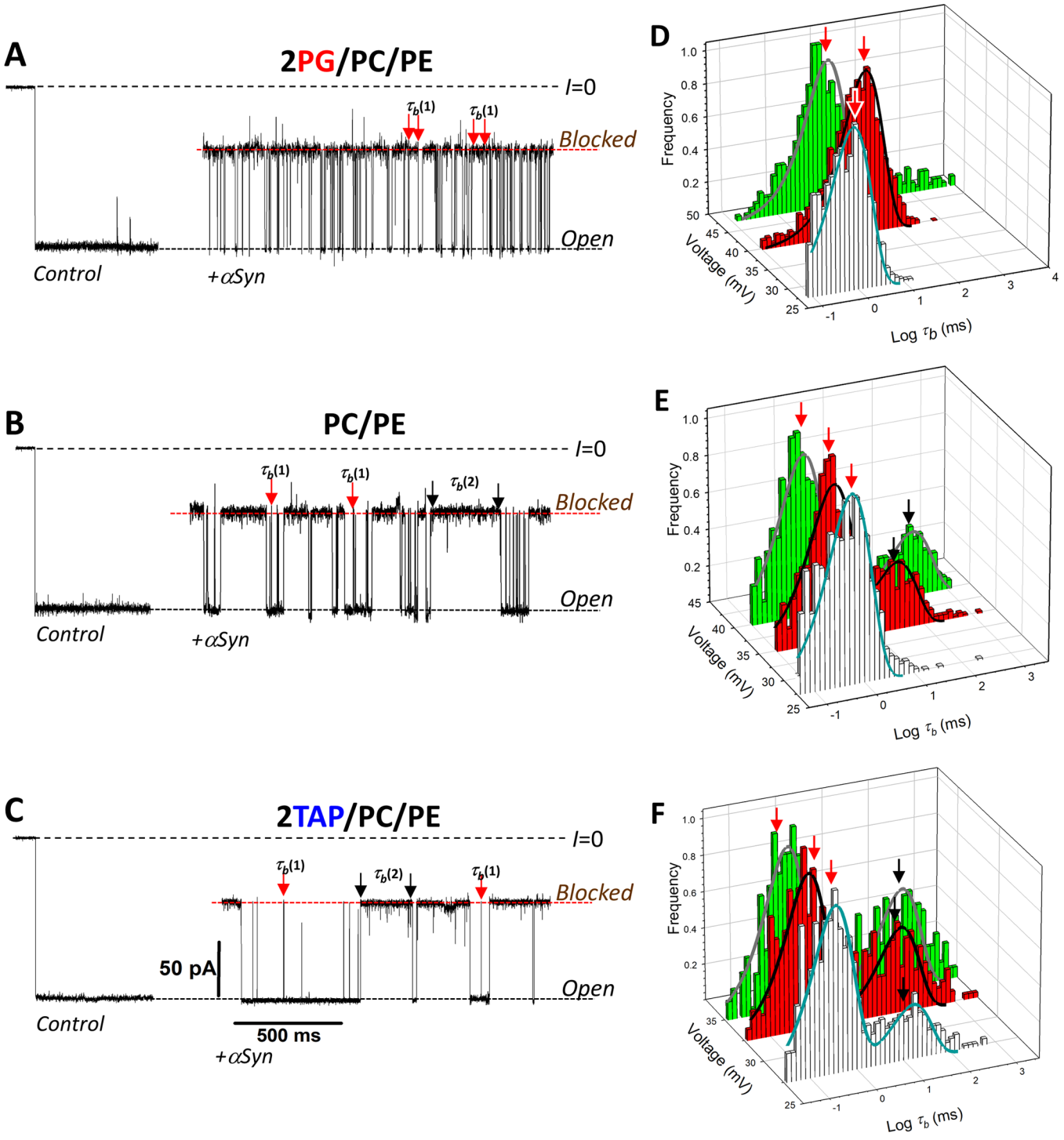

Figure 2. Kinetics of VDAC blockage by αSyn strongly depend on membrane lipid composition. (A–C) Representative current records of VDAC single channels reconstituted into planar membranes formed from lipid mixtures of 2PG/PC/PE (A), PC/PE (B), and 2TAP/PC/PE (C), before (left) and after (right) the addition of 10 nM of αSyn to the *cis* compartment and observed at −37.5 mV of applied voltage. Wide variation in blockage times is detected for a single lipid composition; red arrows indicate short blockage times, $\tau_b^{(1)}$, observed in all three membranes, while black arrows indicate the long-lasting blockage times, $\tau_b^{(2)}$, observed only in PC/PE (B,E) and 2TAP/PC/PE (C,F) membranes but virtually absent in 2PG/PC/PE (A). Horizontal tightly dashed lines indicate VDAC open and blocked by αSyn states; dashed lines indicate zero current. Channel traces were digitally filtered using a 5 kHz low-pass Bessel filter for presentation. The membrane-bathing solution contained 1 M KCl buffered by 5 mM HEPES at pH 7.4. (D–F) Representative log-binned distributions of the blockage times in 2PG/PC/PE (D), PC/PE (E), and 2TAP/PC/PE (F) membranes obtained at three different voltages on each membrane. In anionic 2PG/PC/PE membranes (D), distributions of blockage times are well described by a single-exponential function (solid lines) at all voltages with characteristic times $\tau_{off}^{(1)} = \langle \tau_b^{(1)} \rangle$ indicated by red arrows. In neutral PC/PE membranes (E), a second, longer component of blockage time, $\tau_{off}^{(2)}$, indicated by black arrows, appears at absolute voltages above 32.5 mV. Solid lines in (E,F) are fits to the sum of two exponential functions of τ_b histograms with characteristic times of $\tau_{off}^{(1)}$ and $\tau_{off}^{(2)}$. In cationic 2TAP/PC/PE membranes (F), the longer blockage times (indicated by black arrows) cannot be satisfactorily described by just a single additional exponential function at $|V| > 32.5$ mV.

https://dx.doi.org/10.1021/acsnano.0c07672
ACS Nano 2021, 15, 989−1001

in real time and under a wide range of conditions are essential to understanding these proteins and their biological roles.

In this paper, we demonstrate the use of a single voltage-biased biological nanopore embedded in a lipid bilayer membrane to observe the capture and membrane detachment of intrinsically disordered peripheral membrane proteins or polypeptides at the single-molecule level. We will show that the voltage and time scales at which membrane detachment occurs depend strongly on the lipid composition. The single-molecule nature of this technique reveals a wide variation in the time required for individual proteins to unbind from the same membrane surface, with multiple characteristic dissociation times required to describe this process. Analysis using energy landscape modeling shows that the observed lipid-dependent variation can be attributed to two well-defined physical parameters: the energy of membrane dissociation and the penetration depth or the length of polypeptide that freely penetrates the nanopore trap before being impeded by the membrane anchor. We conclude that the tunable electro-mechanical nanopore trap uncovers a multiplicity of protein binding conformations, each with individual thermodynamic and kinetic signatures that are highly dependent on the composition of the lipid membrane surface.

RESULTS AND DISCUSSION

Determination of Dissociation Rates Using the VDAC Nanopore. A schematic of the strategy for single-molecule determination of the dissociation rate of a peripheral membrane protein is shown in Figure 1. A single nanopore, in this case recombinant murine voltage-dependent anion channel isoform 1 (VDAC), is reconstituted (see Methods) into a lipid bilayer membrane of the desired lipid composition (Figure 1A). VDAC is a 19-stranded β-barrel, weakly anion selective channel that is primarily responsible for transport of multivalent metabolites across the mitochondrial outer membrane (MOM). The membrane separates two reservoirs filled with 1 M KCl (M = mol/L) buffered to pH 7.4 with 5 mM HEPES. A transmembrane voltage V is applied using external electronics coupled to the electrolyte-filled reservoirs using Ag/AgCl electrodes. The ionic current $I(t)$ is continuously recorded. The channel conductance is approximately 4 nS.[14] The channel is prone to gating under applied voltage;[15,16] however, at the relatively small values of V used in these experiments, VDAC behaves as a conventional nanopore, with a low-noise, stable ionic current (Figure 2A).

As a model peripheral membrane protein, we choose α-synuclein (αSyn), a 140-residue intrinsically disordered protein of keen contemporary interest due to its role in the pathology of Parkinson's disease.[17] αSyn has also been shown to modulate the activity of mitochondria *in vivo* due to its interaction with VDAC in the MOM.[18] The VDAC channel is thus the natural choice of nanopore to interrogate membrane-bound αSyn, though the initial characterization of membrane-bound αSyn was performed with the α-hemolysin channel.[19] αSyn has two regions of very different electrostatic charge density (Figure 1B): a 45-residue polyanionic C-terminal domain carries 15 negative elementary charges on the last 37 residues, while the preceding 95 residues are nearly net neutral and are responsible for membrane binding.[20] The membrane binding domain can adopt an α-helical structure on membranes containing anionic or strongly nonlamellar lipids[20−22] but remains disordered when bound to a wide range of other lipids.[23]

The dynamic motion of αSyn in the VDAC nanopore has been extensively characterized and is briefly summarized here.[4,24−26] When αSyn is added to one of the reservoirs contacting the VDAC nanopore, it binds to the membrane surface (Figure 1C). If the voltage has the correct polarity (negative from the side of αSyn addition), the C-terminal domain is then captured into the VDAC nanopore, causing a decrease in the magnitude of the ionic current (shown by † in Figure 1C,D). The anchoring effect of the membrane binding domain prevents the αSyn molecule from immediately passing through the nanopore ("translocating"). Instead, the αSyn molecule stays in the nanopore trap until the C-terminal domain "retracts" (withdraws from the nanopore, driven by stochastic thermal motion), or the membrane anchor dissociates from the membrane surface, allowing the translocation process to proceed.

Either retraction or translocation, marked with * in Figure 1C,D, restore the ionic current to its open pore level. The total trapping duration, from capture to release, is τ_b (Figure 1D). By observing many single molecules of αSyn, distributions of τ_b are constructed (Figure 1E). When the distribution is consistent with a single-exponential distribution characteristic of escape over a high free energy barrier, the single characteristic escape time is $\tau_{off}^{(1)} = \langle \tau_b \rangle$, where the brackets denote an average over individual observations. Otherwise, additional characteristic times ($\tau_{off}^{(2)}$, $\tau_{off}^{(3)}$, ...) may be required to describe the distribution. This has previously been observed with mixtures of polypeptides.[27]

In general, the retraction and translocation processes have different characteristic times, labeled τ_{ret} and τ_{trans}, respectively. The retraction process involves escape over an energy barrier that is largely electrostatic in nature and thus increases linearly with V. As a result, $\tau_{ret}(V) \sim \exp(|V|)$. This is shown as the dashed line on Figure 1F and is denoted the "retraction line". If translocation is impaired (*e.g.*, by a large globular membrane binding domain that cannot pass through the nanopore),[27] this exponential dependence allows many orders of magnitude in τ_{ret} to be explored with modest changes in V.

The translocation time scale $\tau_{trans}(V)$ combines the membrane dissociation time scale and the transit time of αSyn through the nanopore after dissociation. Note that both processes may be voltage-dependent, particularly if membrane binding is destabilized by the tension applied to the αSyn by the transmembrane potential. Indeed, $\tau_{trans}(V)$ is observed to decrease with $|V|$.[25] In electrolyte gradient experiments, the average transit time was measured to be ~0.4 ms.[26] Thus, for $\tau_{trans}(V) \gtrsim 1$ ms, membrane dissociation is the rate-limiting step of translocation, and $\tau_{trans}(V) \approx \tau_d(V)$, where $\tau_d(V)$ is the average time of αSyn dissociation from the membrane.

The probability that an αSyn molecule translocates before retraction occurs is

$$P_{trans}(V) = \frac{\tau_{ret}(V)}{\tau_{ret}(V) + \tau_{trans}(V)} \quad (1)$$

while the average escape time is given by

$$\tau_{off}(V) = P_{trans}(V)\tau_{trans}(V) + (1 - P_{trans}(V))\tau_{ret}(V) \quad (2)$$

As shown in Figure 1F, the qualitatively different voltage dependences of $\tau_{ret}(V)$ and $\tau_{trans}(V)$ lead to a biphasic behavior of $\tau_{off}(V)$ characterized by a crossover potential V^* at the maximum observed escape time, $\tau_{off}(V^*)$.

https://dx.doi.org/10.1021/acsnano.0c07672
ACS Nano 2021, 15, 989−1001

Off-Rates of αSyn−VDAC Interaction in the Membranes of Different Lipid Compositions. The lipids used for bilayer membranes in this study span a wide range of lipid headgroup chemistries. We varied both charge and the headgroup-regulated propensity of the lipids to form lamellar bilayer structures. The particular headgroup choices were focused on lipids that are common in the mitochondrial membranes in which VDAC is found, as well as anionic and nonlamellar lipid species to which αSyn preferentially binds.[21,28] The mammalian MOM is characterized by a high level of phosphatidylcholine (PC) and phosphatidylethanolamine (PE), 55 and 30%, respectively, and by up to ∼15% of anionic lipids, mainly phosphatidylinositol (PI).[29] Here, we use the lipid compositions that closely mimic the high PC (DOPC) and PE (DOPE) content of the MOM, along with 50% of anionic phosphatidylglycerol (DOPG). The positively charged synthetic lipid dioleoyl trimethylammonium propane (DOTAP) was chosen as an antipode of DOPG to study the effect of lipid charge on αSyn−VDAC interaction. Dioleoyl (DO) acyl chains were used uniformly to isolate the effect of the lipid headgroups.

Figure 2A−C shows representative segments of ionic current recordings from a single VDAC channel in the presence of 10 nM αSyn in the membrane-bathing solution, which were obtained on bilayers of three different lipid compositions: anionic DOPG/DOPC/DOPE (2:1:1) (2PG/PC/PE) (A), neutral DOPC/DOPE (1:1) (PC/PE) (B), and cationic DOTAP/DOPC/DOPE (2:1:1) (2TAP/PC/PE) (C). The blockage times τ_b, indicated by arrows in Figure 2A−C, visibly depend on lipid charge, with long-lasting blockage events, labeled $\tau_b^{(2)}$, appearing in the cationic 2TAP/PC/PE (Figure 2C) and neutral PC/PE membranes (Figure 2B). At the same time, the number of blockage events decreases from anionic to neutral to cationic membranes (Figure 2A−C) as was previously shown.[30]

The τ_b distributions show dramatic lipid-dependent differences in the behavior of αSyn in the VDAC nanopore trap. Distributions of τ_b obtained in 2PG/PC/PE membranes are well described by single-exponential functions at all applied voltages (Figure 2D, solid lines); the characteristic dwell times $\tau_{off}^{(1)}(V)$ are shown by red arrows in Figure 2D. In membranes formed from an equimolar mixture of two neutral lipids PC/PE (Figure 2B,E) and in membranes formed from the cationic lipid mixture 2TAP/PC/PE (Figure 2C,F), the τ_b distributions are qualitatively different. In PC/PE membranes, at $|V| > 32.5$ mV (Figure 2E), the populations of short- and long-lasting τ_b are separated by a factor of 20 and can be satisfactorily described by the sum of two single-exponential functions with characteristic times $\tau_{off}^{(1)}$ and $\tau_{off}^{(2)}$, as in Figure 1E. In cationic 2TAP/PC/PE membranes, the τ_b distributions are even more complex (Figure 2F). The long-lasting τ_b have broad distributions, even at the lowest voltages, which require the sum of more than two exponential functions to describe them. As a result, we attempt to characterize only $\tau_{off}^{(1)}$, which has a distinct peak. The long-lasting blockages account for a minor but significant fraction of the total events, about 20 and 30% in PC/PE and 2TAP/PC/PE membranes, respectively.

To assess the effect of lamellar *versus* nonlamellar lipids on the αSyn membrane dissociation rate, we also performed measurements in pure DOPE and DOPC membranes. Single-exponential distributions of τ_b are characteristic for pure DOPE but not for pure DOPC (Figure 3A). For DOPC membranes, the distribution of τ_b requires two-exponential fitting (Figure 3A, right panel, solid lines) with 64 and 36%

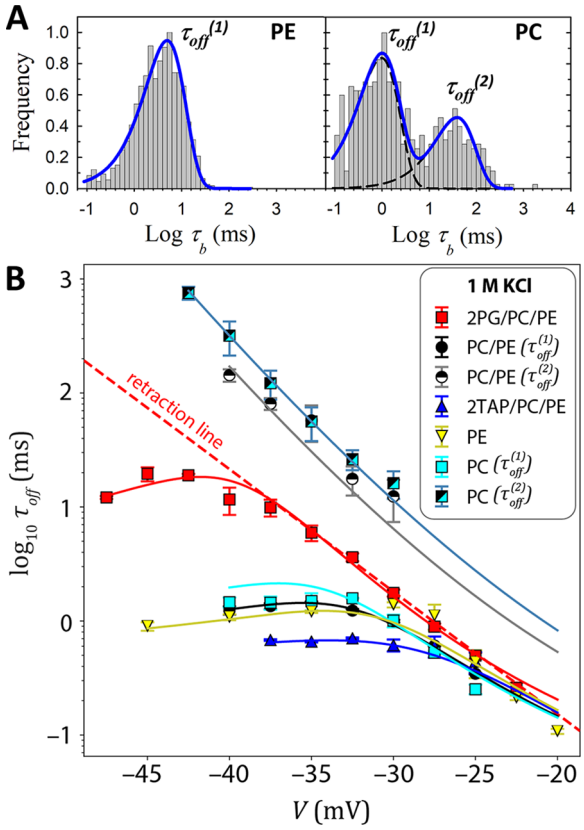

Figure 3. (A) Log-binned distributions of the αSyn−VDAC blockage times τ_b obtained in neutral DOPE (left) and DOPC (right) membranes. The τ_b distributions are fit (solid lines) with a single exponential for DOPE. For DOPC, solid lines are a two-exponential fit, with dashed lines showing the component single-exponential functions describing the short and long-time populations for comparison. Data were obtained at −35 mV. (B) Voltage dependences of $\tau_{off}^{(1)}(V)$ and $\tau_{off}^{(2)}(V)$ for all membrane lipid compositions: 2PG/PC/PE (red), PC/PE (1:1) (black), and 2TAP/PC/PE (blue). Each data point is a mean of 3−5 independent experiments ± standard error (68% confidence interval of the mean). Membrane bathing solutions contained 1 M KCl buffered by 5 mM HEPES to pH 7.4. Solid lines are fits to an energy landscape model (eq 5); the dashed line is an estimate of the retraction line for $\tau_{off}^{(1)}(V)$ for 2PG/PC/PE to guide the eye.

contributions of each exponent to the total distribution of events and well discriminated characteristic times of 1.0 and 39 ms for $\tau_{off}^{(1)}$ and $\tau_{off}^{(2)}$, respectively.

The voltage dependences of $\tau_{off}^{(1)}$ and $\tau_{off}^{(2)}$, where applicable, are shown in Figure 3B for all lipid compositions studied. In each case, $\tau_{off}^{(1)}(V)$ has the characteristic biphasic shape shown in Figure 1F. The retraction lines are similar for all lipid compositions, and the times increase exponentially with V (red dashed line). The departure of τ_{off} from the retraction line changes significantly with lipid content; for example, V^* is approximately −33, −35, and −42 mV in 2TAP/PC/PE, PC/PE, and 2PG/PC/PE membranes, respectively. The associated values of $\tau_{off}^{(1)}(V^*)$ are approximately 0.7, 1.5, and 18 ms, spanning well over an order of magnitude in lipid-dependent membrane dissociation rate. Interestingly, $\tau_{off}^{(1)}(V)$ is essentially the same for DOPE, DOPC, and mixed PC/PE membranes. Thus, $\tau_{off}^{(1)}$ appears to depend strongly on the lipid headgroup charge but is relatively insensitive to the type of the headgroup

https://dx.doi.org/10.1021/acsnano.0c07672
ACS Nano 2021, 15, 989−1001

(PC *vs* PE) and the propensity of the neutral lipid to form nonlamellar structures.

The well-defined exponential distributions of $\tau_b^{(2)}$ in PC/PE and PC membranes allow accurate calculation of $\tau_{off}^{(2)}(V)$, exposing a striking difference with $\tau_{off}^{(1)}(V)$ (Figure 3B). $\tau_{off}^{(2)}$ rises exponentially up to $V = -45$ mV for both PC/PE and PC membranes without deviating from its retraction line; thus, V^* is not achieved within this voltage range and $\tau_{off}^{(2)}$ rises to values that are more than 100 times greater than the maximum $\tau_{off}^{(1)} \approx 2$ ms. The retraction line associated with $\tau_{off}^{(2)}$ is also offset from that of $\tau_{off}^{(1)}$ by a factor of about 4. Together, these results reveal the surprisingly complex nature of αSyn membrane association. While it is to be expected that average membrane dissociation rates differ with membrane composition, the single-molecule approach reveals that even αSyn molecules bound to the same lipid surface have vastly different membrane dissociation rates when interrogated with the VDAC nanopore.

Effect of Electrolyte Concentration. The foregoing experiments were performed under conditions where the lipid and protein charges are largely screened. To further elucidate the role of electrostatics in interactions between the highly negatively charged C-terminus of αSyn and the net positively charged VDAC pore and between the αSyn membrane binding domain and the lipid surface, we explored the effect of lipid charge in a more physiologically relevant 150 mM KCl electrolyte buffer. The results are shown in Figure 4, where

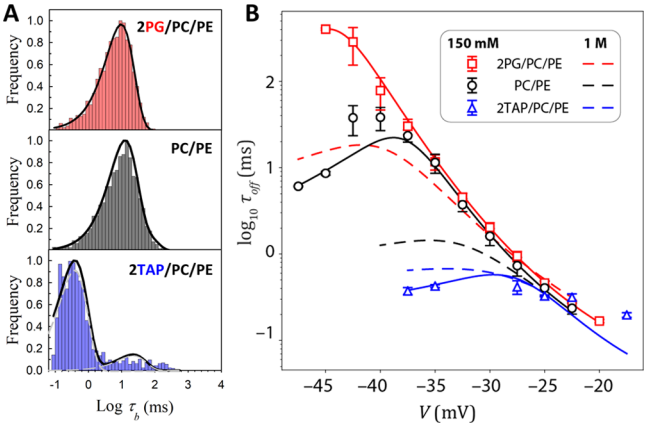

Figure 4. Effect of reduced electrolyte concentration (150 mM KCl). (A) Log-binned distributions of τ_b obtained in 150 mM KCl in 2PG/PC/PE, PC/PE, and 2TAP/PC/PE membranes. Distributions of τ_b in 2PG/PC/PE and PC/PE follow a single exponential (solid line). In the 2TAP/PC/PE membrane, there is a small fraction of longer events, but the distribution is too broad to describe with just two exponential functions (shown individually as dashed lines and their sum as the solid line). All data were obtained at −35 mV. (B) Voltage dependences of $\tau_{off}^{(1)}$. Solid lines are fits to an energy landscape model (eq 5); dashed lines of the same color show the fits to the voltage dependence of $\tau_{off}^{(1)}$ in 1 M KCl (Figure 3B). Each data point is a mean of 3−5 independent experiments ± standard error (68% confidence interval of the mean). Membrane bathing solutions were buffered by 5 mM HEPES at pH 7.4.

two major differences with the data shown in Figures 2 and 3 emerge. First, there is no longer a measurable $\tau_{off}^{(2)}$ in PC/PE membranes at any voltage (Figure 4A, middle panel), and the contribution of the longer times in 2TAP/PC/PE membranes is small but remains too broad for the whole distribution to be described by the sum of just two exponential functions (Figure 4A, lower panel). Therefore, in Figure 4B, we compare only $\tau_{off}^{(1)}(V)$ in 1 M and 150 mM KCl for the three lipid compositions.

Second, $\tau_{off}^{(1)}(V)$ is affected by electrolyte concentration in a lipid-dependent manner (Figure 4B). The retraction lines are independent of ionic strength for all three lipid compositions; however, V^* and $\tau_{off}(V^*)$ depend strongly on electrolyte concentration. In 2PG/PC/PE membranes, V^* is not observed in 150 mM KCl (Figure 4B, red symbols and lines) up to −47.5 mV. In PC/PE membrane, V^* increases from about −33 mV in 1 M KCl to about −38 mV in 150 mM KCl (Figure 4B, black symbols and lines), and $\tau_{off}^{(1)}(V^*)$ increases by an order of magnitude. In 2TAP/PC/PE membranes, the relation between $\tau_{off}^{(1)}(V)$ in high and low salt is reversed in comparison with the two other membranes. In particular, $\tau_{off}^{(1)}(V^*)$ decreases from 1 M KCl to 150 mM KCl (Figure 4B, blue symbols and lines) and is comparable to the 450 μs estimate of the time between membrane dissociation and the completion of the translocation process.[26] This suggests that the membrane anchoring function of the membrane binding domain of αSyn on 2TAP/PC/PE membranes is essentially nonexistent.

Long Membrane Dissociation Times Correspond to Smaller Translocation Probability. For lipid membrane compositions for which αSyn has multiple characteristic dissociation times, the exponential increase of the slower dissociation component is suggestive that these molecules escape primarily by retraction. To demonstrate this, we use a method that allows discrimination of retraction and translocation events on the single-molecule level.[26] Briefly, the VDAC nanopore is subjected to a gradient of electrolyte concentration (Figure 5A). These conditions reveal the altered ionic selectivity of the VDAC channel when the charged or uncharged region of the αSyn molecule is in the channel. Thus, the ionic current reports not only on the presence of an αSyn molecule but also on which domain is in the channel at a given time.[25,26] Of particular interest is the end of each blockage event: if the charged C-terminal domain was in the pore, the molecule retracted, whereas if the uncharged N-terminal domain was in the pore, the molecule translocated. Two such representative blockage events are shown in Figure 5A from an experiment using 10 nM αSyn and a 1:1 DOPC/DOPE lipid membrane with a 0.2 M *cis*/1.0 M *trans* KCl electrolyte gradient. Note that under these conditions, higher voltages are required to observe translocation; that is, V^* increases because the osmotic gradient abets retraction.

When this determination is performed for many individual molecules, histograms of τ_b can be accumulated for events identified as either retractions or translocations, as shown for $V = -47.5$ mV in Figure 5B. As in the symmetric case for a 1:1 DOPC/DOPE membrane, but unlike previous measurements on DPhyPC membranes,[26] the τ_b histograms have two clear components separated at $\tau_b \approx 10$ ms. The τ_b histogram for retraction has characteristic times $\tau_{off}^{(1)} = 2.06 \pm 0.11$ ms and $\tau_{off}^{(2)} = 21.1 \pm 2.4$ ms. The $\tau_{off}^{(1)}$ peak is larger for translocations than for retractions; thus, smaller τ_{off} corresponds primarily to translocations. The opposite is true for $\tau_{off}^{(2)}$ (Figure 5B, inset), which is dominated by retraction events. Thus, the larger τ_{off} corresponds to primarily retraction events. For each τ_b histogram bin, the fraction of translocation events is the observed translocation probability P_{trans}.

The voltage dependences of $\tau_{off}^{(1)}$ and $\tau_{off}^{(2)}$ for retraction events and the dominant $\tau_{off}^{(1)}$ for translocation events are given in Figure 5C, showing the same qualitative features as observed in Figure 3B for PC/PE membranes without the electrolyte gradient. The

https://dx.doi.org/10.1021/acsnano.0c07672
ACS Nano 2021, 15, 989−1001

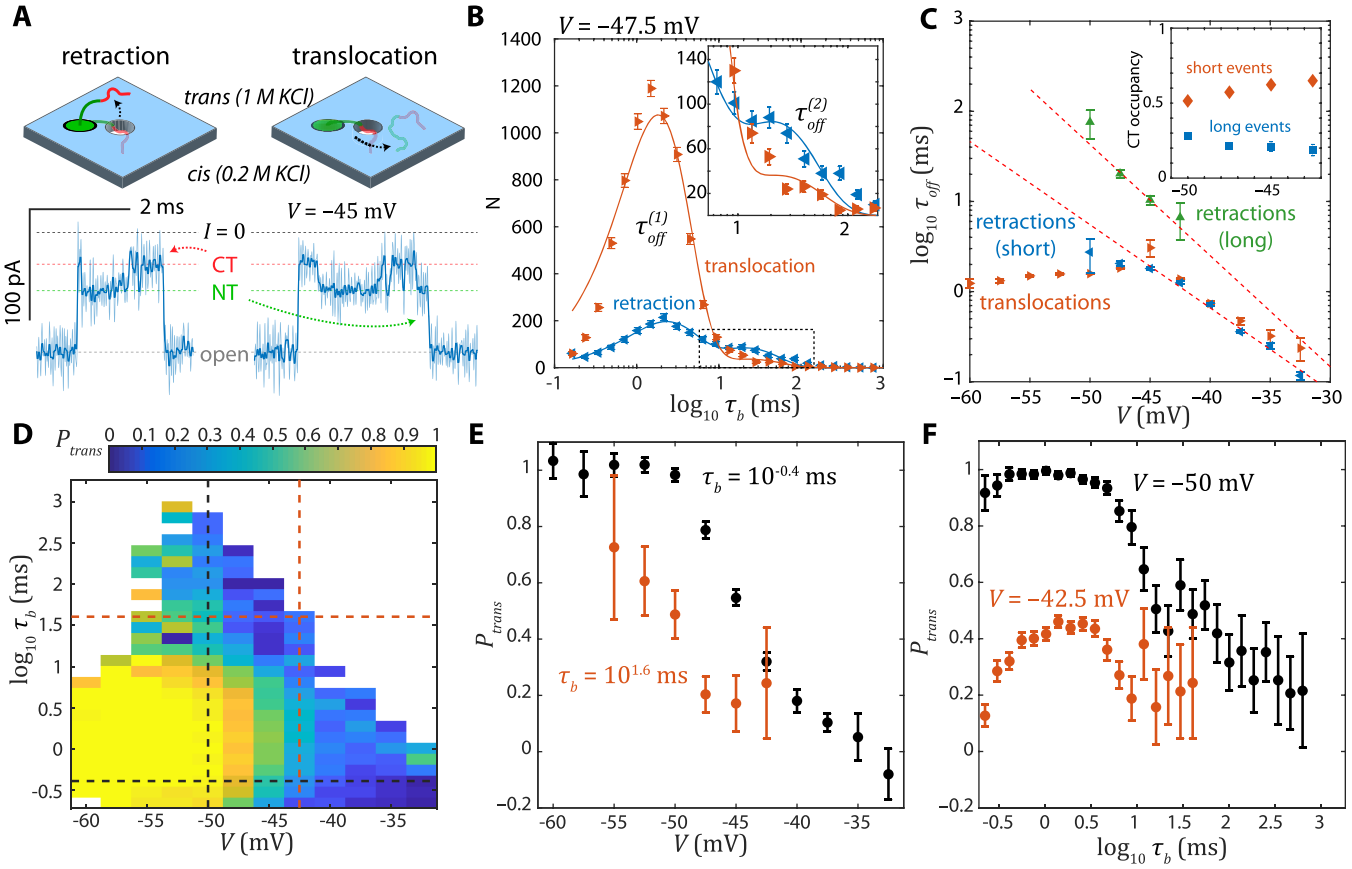

Figure 5. Measurement of translocation probability for αSyn on a 1:1 PC/PE membrane. (A) Identification of single blockage events as retractions or translocations based on the ionic current through the VDAC nanopore at the end of each event. Current traces illustrate one retraction (left) and one translocation (right) event. The two current levels marked by the red and green dashed lines correspond to the presence of the C-terminal (CT) or N-terminal (NT) domains in the nanopore, respectively, and arise from differences in the pore selectivity due to the charge density differences along the αSyn chain. Darker traces show the result of postprocessing with an order 9 median filter. (B) τ_b histograms for retraction and translocation events, showing the presence of $\tau_{off}^{(2)}$ above τ_b = 10 ms. The inset corresponds to the region in the dashed box; the relative incidence of retraction and translocation events is reversed from $\tau_{off}^{(1)}$ to $\tau_{off}^{(2)}$. (C) Voltage dependence of translocation events and short ($\tau_{off}^{(1)}$) and long ($\tau_{off}^{(2)}$) retractions; dashed lines are estimates of the retraction times for the short and long retractions. For long retractions, only data for which $\tau_{off}^{(2)}$ could be determined are included. (Inset) Fraction of time spent by the C-terminal domain in the VDAC nanopore for the short and long events, separated at τ_b = 10 ms. Long events are associated with a lower C-terminal domain occupancy. (D) Dependence of the translocation probability on voltage and blockage time. The probability increases from right to left (increasing |V|) but decreases from bottom to top (increasing blockage time). (E) Translocation probability as a function of voltage at constant observed blockage time. The orange and black data points correspond to the horizontal dashed lines with the same colors in (D). (F) Translocation probability as a function of the observed blockage time at constant voltage. The orange and black data points correspond to the vertical dashed lines with the same colors in (D). Error bars are 68% confidence intervals estimated using bootstrap analysis.

inset displays the average fraction of time spent by the C-terminal domain in the nanopore, showing a large difference between long and short events (both retraction and translocation events were included in this analysis).

Figure 5D gives P_{trans} as a function of both V and τ_b. Cuts through the data shown as vertical and horizontal orange and black dashed lines correspond to the data points of the same color in Figure 5E,F. Figure 5E shows a striking shift to higher voltages in the transition from retraction to translocation when considering events with longer blockage times. The black data points correspond to $\tau_b = 10^{-0.4}$ ms, or $\tau_{off}^{(1)}$, while the orange data correspond to $\tau_b = 10^{1.6}$ ms, or $\tau_{off}^{(2)}$. At a given voltage, the translocation probability is significantly smaller for the data corresponding to $\tau_{off}^{(2)}$, confirming that this peak represents primarily molecules that eventually retract from the VDAC nanopore. Similarly, Figure 5F confirms that, at the same voltage, longer events correspond to a lower translocation probability, that is, are more likely to be retraction events.

Energy Landscape Model of αSyn/VDAC Interaction.

The interaction of αSyn with the VDAC nanopore shown in Figure 1C is complex enough to produce a rich variety of observed behaviors, particularly the biphasic dependence of $\tau_{off}(V)$.[24] The dual charge density regions of αSyn, with its charged C-terminal domain and net uncharged N-terminal domain, provides a molecular fiducial point at the junction that allows the progress of the molecule through the VDAC nanopore to be monitored in real time;[26] this is the basis for the data in Figure 5. These features have allowed the development and validation of free energy landscape models for the αSyn/VDAC interaction.[25] These models have proven quantitatively predictive for the effect of mimic post-translational modifications to αSyn[4] as well as for the interactions of the various disordered C-terminal tails in the plethora of tubulin isotypes with the VDAC nanopore.[27]

Energy landscape modeling entails construction of a one-dimensional free energy profile that describes the interaction

https://dx.doi.org/10.1021/acsnano.0c07672
ACS Nano 2021, 15, 989−1001

energy between a polypeptide and a nanopore and from which a prediction of $\tau_{off}(V)$ can be calculated (Figure 6A). The process is shown in Figure 6B,C. The single spatial dimension, x, represents the length of polypeptide that has threaded through the nanopore constriction. The domain of x runs from 0—when one end of the molecule is in the constriction, and the capture process is beginning or the retraction process completing—to L, the total length of the polypeptide. For αSyn, L = 56 nm, assuming 0.4 nm per amino acid;[31] the boundary between the C-terminal domain and N-terminal domain is at x = 16 nm. At x = L, the translocation process is complete.

The free energy calculation is performed using a Python-based version of the *PPDiffuse* engine.[32] Briefly, the electrokinetic forces are calculated by first converting the amino acid sequence into a linear charge density $\sigma_n(x)$ that responds to V. Hydrodynamic forces from electro-osmotic flow in the nanopore, which arises from the action of the electric field on peptide charge counterions in the pore, are also linear in V, reducing the effective charge density of the peptide to a fraction m_{EOF} of its intrinsic value. Similarly, the nonzero charge density of the pore interior sets up an electro-osmotic flow even in the absence of charge from the polypeptide; this offset is b_{EOF}. Thus, the electric field acts on an *effective* charge density $\sigma_{EOF}(x) = m_{EOF}\sigma_n(x) + b_{EOF}$. For VDAC in 1 M KCl, these values are known from previous studies to be m_{EOF} = 0.659, indicating that electro-osmotic flow cancels about a third of the intrinsic charge density, and b_{EOF} = −0.262 e^-/nm, the effective charge density corresponding to the intrinsic hydrodynamic flow in the VDAC pore. For αSyn in VDAC at −35 mV, the black curve in Figure 6B shows the sum of the electrokinetic free energy profile and an entropic term $U_S(x) = 0.59k_BT[\ln x/L + \ln(1 - x/L)]$. $U_S(x)$ accounts for the multiplicity of molecular configurations at a position x and is small throughout; its maximum magnitude of 3.3 k_BT occurs for the first and last residues only (x = 0.2 nm or x = 55.8 nm).

The membrane dissociation energy profile is modeled as an error function barrier with height E_b, position x_b, and width w_b = 7.13 nm (colored lines in Figure 6B, where w_b = 4 nm for clarity). The height E_b is best interpreted as the activation energy required for membrane dissociation. The position x_b is the penetration depth of the polypeptide and can be considered as the length of the polypeptide that can move freely through the nanopore before its motion is impeded by the membrane anchor. The relatively broad width suggests that the unbinding process may involve a series of fast steps to which the nanopore experiment is not immediately sensitive. This is consistent with the multiple rate constants required to describe unbinding of peptides from lipid bilayer surfaces in force microscopy experiments.[33,34]

The total free energy is the sum of the electrostatic, entropic, and membrane association terms. The expression is

$$U(x) = eV\int_0^x \sigma(x')\mathrm{d}x' + U_S(x) + E_b\mathrm{erf}\left(\frac{x - x_b}{w_b\sqrt{2}}\right) \quad (3)$$

Example curves showing the variation with E_b and x_b are shown in Figure 6C, where the free energy minimum, or trap position, is marked with * for each profile.

At a given time t, the dynamics are described by function $P(x, t; x_0, U(x))$ representing the probability that the system is at x given an initial position x_0 at t = 0. The average escape time $\tau'_{off}(x_0)$ is then calculated as the mean first passage time from the domain of x of a system subject to drift forces represented by

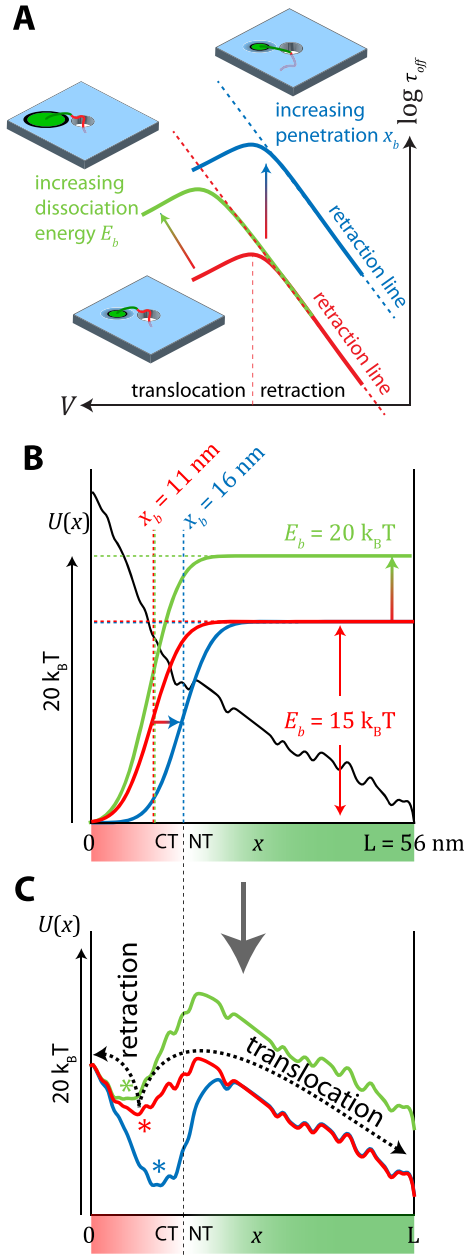

Figure 6. Principles of energy landscape analysis for lipid-dependent membrane dissociation of αSyn. (A) Schematic of the effect on $\tau_{off}(V)$ of the membrane dissociation energy E_b and the penetration depth x_b. (B,C) Construction of the free energy profiles leading to the effects in (A). (B) Electrokinetic free energy was calculated at −35 mV (black curve) and includes entropy. The membrane dissociation free energy is modeled as an error function with height E_b and position x_b. The colored lines show variations with E_b and x_b. E_b is 15 k_BT (red and blue) or 20 k_BT (green); x_b is 11 nm (red and green) or 16 nm (blue). The vertical dashed line shows the boundary at x = 16 nm between the C-terminal domain (CT) and the N-terminal domain (NT). (C) Sum of the electrokinetic free energy and the membrane dissociation free energy profiles in (B) reveals the nanopore trap, marked with *. The heights of the free energy barriers to retraction and to translocation (dashed arrows) depend strongly on E_b and x_b. The free energy barrier to translocation depends primarily on E_b, while the free energy barrier to retraction increases with x_b.

$U(x)$ and with a position-independent diffusion constant D = 0.309 μm^2 s^{-1}. The boundaries at x = 0, L are taken to be

https://dx.doi.org/10.1021/acsnano.0c07672
ACS Nano 2021, 15, 989−1001

absorbing, due to the vanishing probability that a molecule that has retracted or translocated (Figure 6C, dashed arrows) is recaptured by the nanopore. The expression is, for $\tilde{U}(x) = U(x)/k_BT$:[35]

$$D\tau'_{off}(x_0) = \left[\int_0^L dx\left(e^{\tilde{U}(x)}\int_0^x e^{-\tilde{U}(x')}dx'\right)\right]\left[\int_0^{x_0} e^{\tilde{U}(x')}dx'\right]\left[\int_0^L e^{\tilde{U}(x')}dx'\right]^{-1} - \int_0^{x_0} dx\left(e^{\tilde{U}(x)}\int_0^x e^{-\tilde{U}(x')}dx'\right) \quad (4)$$

To avoid dependence on the choice of x_0, the escape times to be compared to experiments are averaged over a distribution $P(x_0)$ of initial positions between 5 and 20 nm, weighted by a Boltzmann distribution, that is, $P(x_0) = e^{-\tilde{U}(x_0)}/\int e^{-\tilde{U}(x_0)}dx_0$. Thus

$$\tau_{off} = \int_{5nm}^{20nm} \tau'_{off}(x_0)P(x_0)dx_0 \quad (5)$$

Of particular interest for the current study is the effect on τ_{off} of the membrane dissociation energy parameters E_b and x_b. This is shown schematically in Figure 6A. Increasing E_b increases the barrier to translocation but does not alter retraction; thus, V^* increases, and $\tau_{off}(V)$ shifts along the retraction line. Increasing x_b, on the other hand, allows more of the charged C-terminal domain to interact with the applied voltage, suppressing retraction and shifting the $\tau_{off}(V)$ curve to larger times and a new retraction line. For the calculations in this article, w_b was fixed at the previously determined 7.1 nm. In this case, the effects of E_b and x_b are not as independent as suggested by Figure 6A, but the general trends remain the same.

Both Membrane Dissociation Energy and Penetration Depth Depend on Lipid Composition. Equation 5 was fit to each $\tau_{off}(V)$ with just two free parameters for each lipid composition, E_b and x_b. The only exception were the data at 150 mM KCl on the 1:1 PC/PE mixture, which were of sufficient quality to additionally determine the electro-osmotic flow parameters for reduced ionic strength. These were determined to be $m_{EOF} = 0.749 \pm 0.068$ and $b_{EOF} = -0.525 \pm 0.049$ (68% confidence intervals). The larger absolute value of m_{EOF} relative to 1 M KCl is consistent with the increased electrical forces at reduced ionic strength, as predicted by Poisson–Boltzmann calculations in solid-state nanopores.[36] On the other hand, at reduced ionic strength the intrinsic charge of the nanopore has a larger effect, as reflected by the increased absolute value of b_{EOF}.

The fit results to eq 5 are shown by the solid lines in Figures 3 and 4B, demonstrating excellent agreement with the experimental $\tau_{off}(V)$, including both $\tau^{(1)}_{off}(V)$ and $\tau^{(2)}_{off}(V)$. The fit parameters are plotted in Figure 7. The horizontal axis shows penetration depth, while the vertical axis is membrane dissociation energy. The inset details the closely clustered points representing most of the observations. Data markers are identical to those used in previous figures and are shown in the legend.

Figure 7 reveals the physical origin of the complex observations reported here. For αSyn on 2PG/PC/PE membranes, the penetration depth is near the boundary between the C-terminal and N-terminal domains, suggesting that the αSyn binding conformation in this case allows the C-terminal domain to almost completely enter the VDAC nanopore. The same is true for PC/PE at 150 mM KCl, but at 1 M KCl, the C-terminal domain penetrates several nanometers less. Most notable is the case of 2TAP/PC/PE in 1 M KCl, where less than

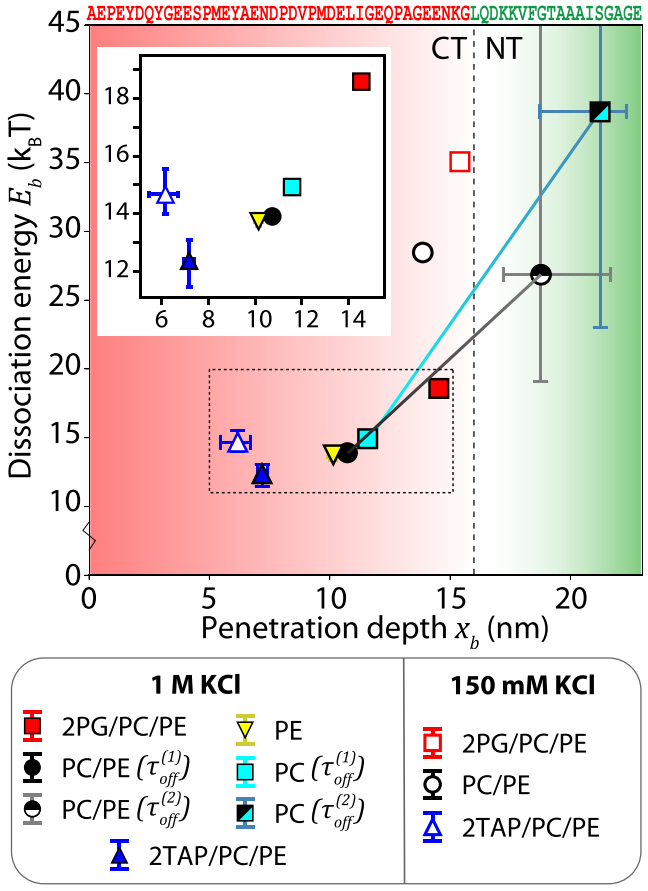

Figure 7. Lipid-dependent membrane dissociation of αSyn is described by two parameters of the energy landscape model, E_b and x_b. All other model parameters were fixed to known values for the VDAC nanopore. Points connected by graded lines show $\tau^{(1)}_{off}$ and $\tau^{(2)}_{off}$ from the same lipid composition. The vertical dashed line shows the boundary between the C-terminal (CT) domain and the N-terminal (NT) domain. Data in the dashed box are shown in greater detail in the inset. Error bars are 95% confidence intervals estimated from posterior distributions of optimized parameters and where not visible are smaller than the data points shown.

half of the C-terminal domain can penetrate the nanopore. A natural explanation is that the anionic C-terminal domain electrostatically binds to the cationic 2TAP/PC/PE surface.

This explanation is borne out by comparing the membrane dissociation energies for 2PG/PC/PE, PC/PE, and 2TAP/PC/PE compositions, with the dissociation constants of 46, 1500, and 116 μM for αSyn on lipid membranes of these compositions in 150 mM KCl determined by fluorescence correlation spectroscopy (FCS).[30] While αSyn binds 2TAP/PC/PE membranes almost as strongly as 2PG/PC/PE membranes, it is apparent from these data that this is almost entirely due to the association of the C-terminal domain with the cationic surface. When the C-terminal domain is sequestered by the nanopore trap, the dissociation energy is significantly reduced relative to that of αSyn on 2PG/PC/PE or PC/PE membranes. The $5k_BT$ difference in dissociation energies for αSyn on 2PG/PC/PE or PC/PE membranes is close to that expected from the natural logarithm of the ratio of dissociation constants, suggesting that at least for these constructs differences in membrane binding strength can be quantified in this manner.

Importantly, the data in Figure 7 show that the accessibility of the C-terminal domain to the nanopore depends significantly on

https://dx.doi.org/10.1021/acsnano.0c07672
ACS Nano 2021, 15, 989−1001

lipid composition, and that this in turn has profound effects on the observed $\tau_{off}^{(1)}(V)$.

Multiple Characteristic Dissociation Times Arise from Disordered Binding Configurations. Perhaps the most striking observation in Figures 2 and 3 is the lipid composition-dependent appearance of a population of αSyn molecules that manifest a very long lifetime, $\tau_{off}^{(2)}(V)$, in the VDAC nanopore. In the experiments reported here, $\tau_{off}^{(2)}$ was observed for PC/PE, 2TAP/PC/PE, and pure PC membranes. It is suggestive that none of these lipid compositions, unlike PE or 2PG/PC/PE,[21,22] are known to induce helical ordering of the membrane binding domain of αSyn.[23] Figure 7 shows the energy landscape modeling results for $\tau_{off}^{(2)}(V)$ in PC/PE and PC membranes. Because the translocation regime is not clearly observed in $\tau_{off}^{(2)}$, the parameters are poorly constrained; however, lower bounds on both parameters can be established and are shown by the edges of the 95% confidence intervals in the plot. For both PC/PE and PC membranes, the penetration depth is such that αSyn is trapped with the uncharged N-terminal domain in the nanopore. This is precisely what is found in the electrolyte gradient experiment (Figure 5C, inset); the occupancy of the C-terminal domain in the VDAC nanopore is significantly reduced for longer events corresponding to $\tau_{off}^{(2)}$. These observations are consistent with a disordered binding configuration that, unlike the binding configuration leading to $\tau_{off}^{(1)}$, allows the C-terminal domain to fully pass through the VDAC nanopore constriction, so the trapped molecule does not experience the strong electrical forces that would enhance membrane dissociation by acting on the highly charged C-terminal domain. Thus, $\tau_{off}^{(2)}$ reveals the presence of two (or more) distinct binding conformations populated by αSyn molecules on the same membrane surface. Depending on its binding conformation, the observed dynamics of αSyn in the VDAC nanopore trap, and particularly the release of αSyn from the membrane surface, differ by orders of magnitude, as revealed by the single-molecule measurement.

Comparison of E_b for $\tau_{off}^{(2)}$ and $\tau_{off}^{(1)}$ for the same compositions (see the graded lines connecting each pair of PC and PC/PE membrane data points in Figure 7) shows that the membrane dissociation energy corresponding to $\tau_{off}^{(2)}$ is at least 5 k_BT greater than that of $\tau_{off}^{(1)}$. It is counterintuitive that binding conformations that allow αSyn to penetrate further into the VDAC nanopore have a larger apparent binding energy, as less polypeptide would then be available to interact with the lipid surface, but it is by no means impossible. One source of apparent excess binding energy may be the nature of a disordered binding domain, which may spread its binding energy over individual subdomains that interact with the lipid surface.[37] Each subdomain is in a dynamic equilibrium between bound and dissociated states. All subdomains must simultaneously dissociate for the molecule to translocate, in principle leading to very slow unbinding kinetics that in the context of the energy landscape model would be interpreted as binding energy. This "false stability", in which αSyn is stabilized on the membrane surface despite only a modest binding energy, would be advantageous for a cell because it could efficiently regulate VDAC with relatively few protein copies. Further experiments and computational studies will be invaluable in identifying the role of disorder in lipid-dependent αSyn binding conformations and kinetics.

An alternative but equally likely source of excess dissociation energy for $\tau_{off}^{(2)}$ is αSyn oligomerization on the lipid surface. Oligomer association could provide both the additional membrane binding energy and the C-terminal tail accessibility deduced from the energy landscape modeling. The lipid dependence would then reflect the ability of lipid membrane surfaces of differing compositions to either maintain bound oligomeric structures or reorganize oligomeric αSyn from solution into membrane-bound monomers.[38,39] Lipid-mediated protein−protein interactions are of particular interest for the biology of the MOM, which is the point of contact between mitochondria and other organelle membranes, such as the endoplasmic or sarcoplasmic reticulum, and is where regulation of calcium transport to mitochondria, lipid metabolism, and mitochondrial quality control take place.[40−43] Lipid−protein interactions mediate the association of various cytosolic proteins such as glycolytic enzymes, hexokinase, and cytoskeletal and neuronal proteins with the MOM[18,44−47] and participate in apoptotic execution happening directly at the outer membrane.[48] As in the study reported here, a local nanopore probe in a biomimetic MOM may serve as a sensitive electromechanical trap to measure the effect of lipids on transient interactions between mitochondrial and cytosolic proteins involved in metabolic and survival pathways.

Furthermore, these results may have profound implications for the role of αSyn in regulating the fluxes of anionic metabolites through the VDAC channel.[18,49] It is tempting to speculate that the long-lived αSyn VDAC blockages—by the molecules whose conformation limits translocation—are more effective in controlling metabolite flux *in vivo*. At the same time, the short-lived αSyn VDAC blockages—by the molecules in a different conformation—correspond to a higher probability of αSyn translocation through VDAC and subsequent impairment of the electron transport complexes located in the inner membrane, thus causing mitochondrial dysfunction.[18,45,50] The findings presented here suggest that the membrane lipid composition modulates the relative populations of αSyn molecules in different conformations on the surface of the outer membrane, thus tuning the average response of VDAC and mitochondria to αSyn. This mechanism suggests that the two populations of αSyn have significantly different unbinding kinetics in the absence of applied force from the nanopore; future complementary measurements on a similar system will be invaluable in determining whether this condition is met.

CONCLUSIONS

We have shown that the VDAC nanopore embedded in a voltage-biased phospholipid bilayer membrane creates an electromechanical trap to study mechanistic features of membrane-bound αSyn dissociation. The αSyn molecule remains trapped until one of two slow events occurs: its charged C-terminal domain escapes due to stochastic thermal forces acting against the electrical forces, or its membrane binding domain detaches from the surface, allowing translocation to proceed. The trap depth is tunable via the transmembrane potential, allowing orders of magnitude of characteristic escape times to be explored. The measurement reveals that the membrane dissociation time is very sensitive to the membrane phospholipid composition. Surprisingly, for certain compositions, the dissociation of αSyn from the *same* lipid membranes obeys multiple characteristic rates, suggesting the presence of multiple binding conformations of the protein on the surface. Each binding conformation can be parametrized by two physical quantities: the membrane dissociation free energy, and the length of the αSyn polypeptide that is available to penetrate the pore before being arrested by the membrane binding domain.

https://dx.doi.org/10.1021/acsnano.0c07672
ACS Nano 2021, 15, 989−1001

In sum, an electromechanical trap such as that described here provides a local, single-molecule probe of dissociation kinetics of membrane-bound proteins. The results presented in this work have profound implications for our understanding of protein−lipid interactions, and particularly the roles that disordered membrane binding domains and their inherent stochasticity play in recruiting peripheral proteins to, and preventing their exit from, the surfaces of phospholipid membranes.

METHODS

Protein Purification. Recombinant mouse VDAC1 (VDAC) was a kind gift of Dr. Adam Kuszak (Laboratory of Chemical Physics, NIDDK, NIH). VDAC1 was expressed, refolded, and purified using a protocol described previously.[30,51] αSyn WT was a generous gift of Dr. Jennifer Lee (NHLBI, NIH, Bethesda, USA). αSyn was expressed, purified, and characterized as previously described.[24]

Channel Reconstitution. The mixtures of lipids were prepared from 10 mg/mL aliquots of two or three lipid solutions in chloroform, followed by drying with nitrogen and then redissolving them in pentane to a total lipid concentration of 5 mg/mL. 1,2-Dioleoyl-*sn*-glycero-3-phosphocholine (DOPC), 1,2-dioleoyl-*sn*-glycero-3-phosphoethanolamine (DOPE), 1,2-dioleoyl-*sn*-glycero-3-phospho-(1′-*rac*-glycerol) (DOPG), and 1,2-dioleoyl-3-trimethylammonium propane (DOTAP) were purchased from Avanti Polar Lipids (Alabaster, AL). Planar bilayer membranes were formed from two opposing lipid monolayers across a ∼70 μm aperture in the 15 μm thick Teflon partition separating two ∼1.2 mL compartments as previously described.[52] VDAC insertion was achieved by adding recombinant murine VDAC1 in 2.5% Triton X-100 buffer[53] to the aqueous phase of 1 M or 150 mM KCl buffered with 5 mM HEPES at pH 7.4 in the *cis* compartment. Potential is defined as positive when it is greater at the side of VDAC addition (*cis*). αSyn at a final concentration of 10 nM was added symmetrically to the both sides of the membrane after VDAC channel reconstitution. The low concentration of αSyn suppressed simultaneous capture of multiple αSyn molecules.[25] In selectivity experiments, the *trans* side was filled with a solution of 1.0 M KCl and the *cis* side with a 0.2 M KCl solution, both buffered with 5 mM HEPES at pH 7.4. αSyn was added to the *trans* side at 5 nM concentration. Junction potentials with the Ag/AgCl electrodes were minimized because in all experiments the electrodes were connected *via* 2 M KCl/2% agarose bridges.

Conductance measurements were performed as described previously[24] using an Axopatch 200B amplifier (Axon Instruments, Inc., Foster City, CA) in the voltage clamp mode. Data were filtered by a low-pass 8-pole Butterworth filter (model 900, Frequency Devices, Inc., Haverhill, MA) at 15 kHz and a low-pass Bessel filter at 10 kHz and directly saved into computer memory with a sampling frequency of 50 kHz.

Open and Blockage Times Analysis. For data analysis by Clampfit 10.3, a digital 8-pole Bessel low-pass filter set at 5 or 2 kHz was applied to current recordings in 1 M KCl and 150 mM KCl, respectively, and then individual events of current blockages were discriminated and kinetic parameters were acquired by fitting single exponentials to logarithmically binned histograms[54] as described previously.[24,55] Four different logarithmic probability fits were generated using different fitting algorithms, and the mean of the fitted time constants was used as the mean for the characteristic open and blockage times. Each channel experiment was repeated 3−7 times on different membranes. Statistical analysis of the blockage events began 15 min after αSyn addition to ensure a steady state. Rare VDAC gating events have a different current blockage amplitude and are much longer than blockages associated with αSyn and were thus easily eliminated from the analysis.

Data analysis in selectivity experiments was performed as described previously.[26] αSyn capture and release processes were detected with a threshold algorithm. A threshold was set at 0.75 times the open pore current at each applied voltage. Captures were detected when the absolute current level dropped below the threshold; releases (due to either retraction or translocation) are recorded when the absolute current level rose above the threshold. An "event" was defined as the time between a capture and its subsequent release. Data sampled at 4 μs were filtered with a median filter (order 21) such that the minimum event length was approximately 80 μs. Average currents were calculated by fitting a Gaussian function to a histogram of the filtered current for each voltage. These average currents were then used to differentiate between sublevels of each event corresponding to occupancy of VDAC by the C-terminal or N-terminal domain of αSyn.

Modeling and Optimization. The model was implemented using custom Python code. Optimization was performed on the Bridges[56,57] high-performance computing system using the DREAM Markov Chain Monte Carlo (MCMC) algorithm[58] implemented in the software package *Bumps*.[59] Confidence intervals on parameters and model predictions are calculated from the last 24,528 of at least 744,528 total DREAM samples.

AUTHOR INFORMATION

Corresponding Author

David P. Hoogerheide − *Center for Neutron Research, National Institute of Standards and Technology, Gaithersburg, Maryland 20899, United States;* orcid.org/0000-0003-2918-1469; Email: david.hoogerheide@nist.gov

Authors

Tatiana K. Rostovtseva − *Section on Molecular Transport, Eunice Kennedy Shriver National Institute of Child Health and Human Development, National Institutes of Health, Bethesda, Maryland 20892, United States*

Daniel Jacobs − *Section on Molecular Transport, Eunice Kennedy Shriver National Institute of Child Health and Human Development, National Institutes of Health, Bethesda, Maryland 20892, United States*

[§]**Philip A. Gurnev** − *Section on Molecular Transport, Eunice Kennedy Shriver National Institute of Child Health and Human Development, National Institutes of Health, Bethesda, Maryland 20892, United States;* orcid.org/0000-0001-9247-5027

Sergey M. Bezrukov − *Section on Molecular Transport, Eunice Kennedy Shriver National Institute of Child Health and Human Development, National Institutes of Health, Bethesda, Maryland 20892, United States;* orcid.org/0000-0002-8209-8050

Complete contact information is available at: https://pubs.acs.org/10.1021/acsnano.0c07672

Notes

The authors declare no competing financial interest.

[§]Deceased, August 5, 2019.

ACKNOWLEDGMENTS

Authors thank J. Lee (NHLBI, NIH) for providing αSyn and A. Kuszak (NIDDK, NIH) for providing VDAC1. This work used the Extreme Science and Engineering Discovery Environment (XSEDE), which is supported by National Science Foundation Grant No. ACI-1053575. Specifically, it used the Bridges system, which is supported by NSF award number ACI-1445606, at the Pittsburgh Supercomputing Center (PSC). P.A.G., T.K.R., and S.M.B. were supported by the Intramural Research Program of the *Eunice Kennedy Shriver* National Institute of Child Health and Human Development, NIH. Certain commercial materials, equipment, and instruments are identified in this work to describe the experimental procedure as completely as possible. In no case does such an identification imply a recommendation or endorsement by NIST, nor does it imply that the materials,

https://dx.doi.org/10.1021/acsnano.0c07672
ACS Nano 2021, 15, 989−1001

equipment, or instrument identified are necessarily the best available for the purpose.

REFERENCES

(1) Yusko, E. C.; Johnson, J. M.; Majd, S.; Prangkio, P.; Rollings, R. C.; Li, J.; Yang, J.; Mayer, M. Controlling Protein Translocation through Nanopores with Bio-Inspired Fluid Walls. *Nat. Nanotechnol.* **2011**, *6*, 253−60.

(2) Dong, Z.; Kennedy, E.; Hokmabadi, M.; Timp, G. Discriminating Residue Substitutions in a Single Protein Molecule Using a Sub-Nanopore. *ACS Nano* **2017**, *11*, 5440−52.

(3) Nivala, J.; Marks, D. B.; Akeson, M. Unfoldase-Mediated Protein Translocation through an α-Hemolysin Nanopore. *Nat. Biotechnol.* **2013**, *31*, 247−50.

(4) Hoogerheide, D. P.; Gurnev, P. A.; Rostovtseva, T. K.; Bezrukov, S. M. Effect of a Post-Translational Modification Mimic on Protein Translocation through a Nanopore. *Nanoscale* **2020**, *12*, 11070−78.

(5) Thakur, A. K.; Movileanu, L. Real-Time Measurement of Protein−Protein Interactions at Single-Molecule Resolution Using a Biological Nanopore. *Nat. Biotechnol.* **2019**, *37*, 96−101.

(6) Callahan, N.; Tullman, J.; Kelman, Z.; Marino, J. Strategies for Development of a Next-Generation Protein Sequencing Platform. *Trends Biochem. Sci.* **2020**, *45*, 76−89.

(7) Restrepo-Pérez, L.; Joo, C.; Dekker, C. Paving the Way to Single-Molecule Protein Sequencing. *Nat. Nanotechnol.* **2018**, *13*, 786−96.

(8) Ouldali, H.; Sarthak, K.; Ensslen, T.; Piguet, F.; Manivet, P.; Pelta, J.; Behrends, J. C.; Aksimentiev, A.; Oukhaled, A. Electrical Recognition of the Twenty Proteinogenic Amino Acids Using an Aerolysin Nanopore. *Nat. Biotechnol.* **2020**, *38*, 176−81.

(9) Almen, M. S.; Nordstrom, K. J.; Fredriksson, R.; Schioth, H. B. Mapping the Human Membrane Proteome: A Majority of the Human Membrane Proteins Can Be Classified According to Function and Evolutionary Origin. *BMC Biol.* **2009**, *7*, 50.

(10) Yildirim, M. A.; Goh, K.-I.; Cusick, M. E.; Barabasi, A.-L.; Vidal, M. Drug-Target Network. *Nat. Biotechnol.* **2007**, *25*, 1119−26.

(11) Johnson, J. E.; Cornell, R. B. Amphitropic Proteins: Regulation by Reversible Membrane Interactions (Review). *Mol. Membr. Biol.* **1999**, *16*, 217−35.

(12) Scott, J. L.; Musselman, C. A.; Adu-Gyamfi, E.; Kutateladze, T. G.; Stahelin, R. V. Emerging Methodologies to Investigate Lipid−Protein Interactions. *Integrative Biology* **2012**, *4*, 247−58.

(13) Tatulian, S. A. Interfacial Enzymes: Membrane Binding, Orientation, Membrane Insertion, and Activity. In *Enzymology at the Membrane Interface: Interfacial Enzymology and Protein-Membrane Binding*, 1st ed.; Gelb, M. H., Ed.; Methods in Enzymology; Academic Press: Cambridge, MA, 2017; Vol. *583*, Chapter 9, pp 197−230.

(14) Rostovtseva, T. K.; Gurnev, P. A.; Hoogerheide, D. P.; Rovini, A.; Sirajuddin, M.; Bezrukov, S. M. Sequence Diversity of Tubulin Isotypes in Regulation of the Mitochondrial Voltage-Dependent Anion Channel. *J. Biol. Chem.* **2018**, *293*, 10949−62.

(15) Colombini, M. Candidate for the Permeability Pathway of the Outer Mitochondrial-Membrane. *Nature* **1979**, *279*, 643−45.

(16) Rappaport, S. M.; Teijido, O.; Hoogerheide, D. P.; Rostovtseva, T. K.; Berezhkovskii, A. M.; Bezrukov, S. M. Conductance Hysteresis in the Voltage-Dependent Anion Channel. *Eur. Biophys. J.* **2015**, *44*, 465−72.

(17) Nussbaum, R. L. Genetics of Synucleinopathies. *Cold Spring Harbor Perspect. Med.* **2018**, *8*, a024109.

(18) Rovini, A.; Gurnev, P. A.; Beilina, A.; Queralt-Martin, M.; Rosencrans, W.; Cookson, M. R.; Bezrukov, S. M.; Rostovtseva, T. K. Molecular Mechanism of Olesoxime-Mediated Neuroprotection through Targeting Alpha-Synuclein Interaction with Mitochondrial VDAC. *Cell. Mol. Life Sci.* **2020**, *77*, 3611−26.

(19) Gurnev, P. A.; Yap, T. L.; Pfefferkorn, C. M.; Rostovtseva, T. K.; Berezhkovskii, A. M.; Lee, J. C.; Parsegian, V. A.; Bezrukov, S. M. Alpha-Synuclein Lipid-Dependent Membrane Binding and Translocation through the Alpha-Hemolysin Channel. *Biophys. J.* **2014**, *106*, 556−65.

(20) Eliezer, D.; Kutluay, E.; Bussell, R., Jr.; Browne, G. Conformational Properties of Alpha-Synuclein in Its Free and Lipid-Associated States. *J. Mol. Biol.* **2001**, *307*, 1061−73.

(21) Pfefferkorn, C. M.; Jiang, Z.; Lee, J. C. Biophysics of Alpha-Synuclein Membrane Interactions. *Biochim. Biophys. Acta, Biomembr.* **2012**, *1818*, 162−71.

(22) Jo, E.; McLaurin, J.; Yip, C. M.; St. George-Hyslop, P.; Fraser, P. E. Alpha-Synuclein Membrane Interactions and Lipid Specificity. *J. Biol. Chem.* **2000**, *275*, 34328−34.

(23) O'Leary, E. I.; Jiang, Z.; Strub, M. P.; Lee, J. C. Effects of Phosphatidylcholine Membrane Fluidity on the Conformation and Aggregation of N-Terminally Acetylated Alpha-Synuclein. *J. Biol. Chem.* **2018**, *293*, 11195−205.

(24) Rostovtseva, T. K.; Gurnev, P. A.; Protchenko, O.; Hoogerheide, D. P.; Yap, T. L.; Philpott, C. C.; Lee, J. C.; Bezrukov, S. M. Alpha-Synuclein Shows High Affinity Interaction with Voltage-Dependent Anion Channel, Suggesting Mechanisms of Mitochondrial Regulation and Toxicity in Parkinson Disease. *J. Biol. Chem.* **2015**, *290*, 18467−77.

(25) Hoogerheide, D. P.; Gurnev, P. A.; Rostovtseva, T. K.; Bezrukov, S. M. Mechanism of Alpha-Synuclein Translocation through a VDAC Nanopore Revealed by Energy Landscape Modeling of Escape Time Distributions. *Nanoscale* **2017**, *9*, 183−92.

(26) Hoogerheide, D. P.; Gurnev, P. A.; Rostovtseva, T. K.; Bezrukov, S. M. Real-Time Nanopore-Based Recognition of Protein Translocation Success. *Biophys. J.* **2018**, *114*, 772−76.

(27) Rostovtseva, T. K.; Gurnev, P. A.; Hoogerheide, D. P.; Rovini, A.; Sirajuddin, M.; Bezrukov, S. M. Sequence Diversity of Tubulin Isotypes in Regulation of the Mitochondrial Voltage-Dependent Anion Channel. *J. Biol. Chem.* **2018**, *293*, 10949−62.

(28) Davidson, W. S.; Jonas, A.; Clayton, D. F.; George, J. M. Stabilization of Alpha-Synuclein Secondary Structure Upon Binding to Synthetic Membranes. *J. Biol. Chem.* **1998**, *273*, 9443−9.

(29) Horvath, S. E.; Daum, G. Lipids of Mitochondria. *Prog. Lipid Res.* **2013**, *52*, 590−614.

(30) Jacobs, D.; Hoogerheide, D. P.; Rovini, A.; Jiang, Z.; Lee, J. C.; Rostovtseva, T. K.; Bezrukov, S. M. Probing Membrane Association of Alpha-Synuclein Domains with VDAC Nanopore Reveals Unexpected Binding Pattern. *Sci. Rep.* **2019**, *9*, 4580.

(31) Ainavarapu, S. R. K.; Brujić, J.; Huang, H. H.; Wiita, A. P.; Lu, H.; Li, L.; Walther, K. A.; Carrion-Vazquez, M.; Li, H.; Fernandez, J. M. Contour Length and Refolding Rate of a Small Protein Controlled by Engineered Disulfide Bonds. *Biophys. J.* **2007**, *92*, 225−33.

(32) Hoogerheide, D. P. PPDiffuse: A Quantitative Prediction Tool for Diffusion of Charged Polymers in a Nanopore. *J. Res. Natl. Inst Stan* **2020**, *125*, 125018.

(33) Matin, T. R.; Sigdel, K. P.; Utjesanovic, M.; Marsh, B. P.; Gallazzi, F.; Smith, V. F.; Kosztin, I.; King, G. M. Single-Molecule Peptide−Lipid Affinity Assay Reveals Interplay between Solution Structure and Partitioning. *Langmuir* **2017**, *33*, 4057−65.

(34) Utjesanovic, M.; Matin, T. R.; Sigdel, K. P.; King, G. M.; Kosztin, I. Multiple Stochastic Pathways in Forced Peptide-Lipid Membrane Detachment. *Sci. Rep.* **2019**, *9*, 451.

(35) van Kampen, N. G. *Stochastic Processes in Physics and Chemistry*, 3rd ed.; Elsevier: Amsterdam, 2007.

(36) Lu, B.; Hoogerheide, D. P.; Zhao, Q.; Yu, D. P. Effective Driving Force Applied on DNA inside a Solid-State Nanopore. *Phys. Rev. E* **2012**, *86*, No. 011921.

(37) Mosior, M.; Mclaughlin, S. Electrostatics and Reduction of Dimensionality Produce Apparent Cooperativity When Basic Peptides Bind to Acidic Lipids in Membranes. *Biochim. Biophys. Acta, Biomembr.* **1992**, *1105*, 185−87.

(38) Comellas, G.; Lemkau, L. R.; Zhou, D. H. H.; George, J. M.; Rienstra, C. M. Structural Intermediates during Alpha-Synuclein Fibrillogenesis on Phospholipid Vesicles. *J. Am. Chem. Soc.* **2012**, *134*, 5090−99.

(39) Bodner, C. R.; Maltsev, A. S.; Dobson, C. M.; Bax, A. Differential Phospholipid Binding of Alpha-Synuclein Variants Implicated in Parkinson's Disease Revealed by Solution NMR Spectroscopy. *Biochemistry* **2010**, *49*, 862−71.

https://dx.doi.org/10.1021/acsnano.0c07672
ACS Nano 2021, 15, 989−1001

(40) Csordás, G.; Várnai, P.; Golenár, T.; Roy, S.; Purkins, G.; Schneider, T. G.; Balla, T.; Hajnóczky, G. Imaging Interorganelle Contacts and Local Calcium Dynamics at the ER-Mitochondrial Interface. *Mol. Cell* **2010**, *39*, 121−32.
(41) Kannan, M.; Lahiri, S.; Liu, L.-K.; Choudhary, V.; Prinz, W. A. Phosphatidylserine Synthesis at Membrane Contact Sites Promotes Its Transport out of the ER. *J. Lipid Res.* **2017**, *58*, 553−62.
(42) McLelland, G.-L.; Goiran, T.; Yi, W.; Dorval, G.; Chen, C. X.; Lauinger, N. D.; Krahn, A. I.; Valimehr, S.; Rakovic, A.; Rouiller, I.; Durcan, T. M.; Trempe, J.-F.; Fon, E. A. Mfn2 Ubiquitination by PINK1/Parkin Gates the p97-Dependent Release of ER from Mitochondria to Drive Mitophagy. *eLife* **2018**, *7*, e32866.
(43) Perrone, M.; Caroccia, N.; Genovese, I.; Missiroli, S.; Modesti, L.; Pedriali, G.; Vezzani, B.; Vitto, V. A. M.; Antenori, M.; Lebiedzinska-Arciszewska, M.; Wieckowski, M. R.; Giorgi, C.; Pinton, P. The Role of Mitochondria-Associated Membranes in Cellular Homeostasis and Diseases. In *Biology of the Endoplasmic Reticulum*, 1st ed.; Kepp, O., Galluzzi, L., Eds.; International Review of Cell and Molecular Biology; Academic Press: Cambridge, MA, 2020; Vol. *350*, Chapter 4, pp 119−96.
(44) Al Jamal, J. A. Involvement of Porin N,N-Dicyclohexylcarbodiimide-Reactive Domain in Hexokinase Binding to the Outer Mitochondrial Membrane. *Protein J.* **2005**, *24*, 1−8.
(45) Gouarné, C.; Tracz, J.; Paoli, M. G.; Deluca, V.; Seimandi, M.; Tardif, G.; Xilouri, M.; Stefanis, L.; Bordet, T.; Pruss, R. M. Protective Role of Olesoxime against Wild-Type A-Synuclein-Induced Toxicity in Human Neuronally Differentiated Shsy-5y Cells. *Br. J. Pharmacol.* **2015**, *172*, 235−45.
(46) Magrì, A.; Belfiore, R.; Reina, S.; Tomasello, M. F.; Di Rosa, M. C.; Guarino, F.; Leggio, L.; De Pinto, V.; Messina, A. Hexokinase I N-Terminal Based Peptide Prevents the VDAC1-SOD1 G93a Interaction and Re-Establishes ALS Cell Viability. *Sci. Rep.* **2016**, *6*, 34802.
(47) Rostovtseva, T. K.; Sheldon, K. L.; Hassanzadeh, E.; Monge, C.; Saks, V.; Bezrukov, S. M.; Sackett, D. L. Tubulin Binding Blocks Mitochondrial Voltage-Dependent Anion Channel and Regulates Respiration. *Proc. Natl. Acad. Sci. U. S. A.* **2008**, *105*, 18746−51.
(48) Chipuk, J. E.; Bouchier-Hayes, L.; Green, D. R. Mitochondrial Outer Membrane Permeabilization during Apoptosis: The Innocent Bystander Scenario. *Cell Death Differ.* **2006**, *13*, 1396−402.
(49) Rostovtseva, T. K.; Hoogerheide, D. P.; Rovini, A.; Bezrukov, S. M. Lipids in Regulation of the Mitochondrial Outer Membrane Permeability, Bioenergetics, and Metabolism. In *Molecular Basis for Mitochondrial Signaling*; Rostovtseva, T. K., Ed.; Springer International Publishing: Cham, 2017; pp 185−215.
(50) Ludtmann, M. H. R.; Angelova, P. R.; Ninkina, N. N.; Gandhi, S.; Buchman, V. L.; Abramov, A. Y. Monomeric Alpha-Synuclein Exerts a Physiological Role on Brain ATP Synthase. *J. Neurosci.* **2016**, *36*, 10510−21.
(51) Ujwal, R.; Cascio, D.; Colletier, J.-P.; Faham, S.; Zhang, J.; Toro, L.; Ping, P.; Abramson, J. The Crystal Structure of Mouse VDAC1 at 2.3 A Resolution Reveals Mechanistic Insights into Metabolite Gating. *Proc. Natl. Acad. Sci. U. S. A.* **2008**, *105*, 17742−47.
(52) Rostovtseva, T. K.; Gurnev, P. A.; Chen, M. Y.; Bezrukov, S. M. Membrane Lipid Composition Regulates Tubulin Interaction with Mitochondrial Voltage-Dependent Anion Channel. *J. Biol. Chem.* **2012**, *287*, 29589−98.
(53) Eddy, M. T.; Ong, T. C.; Clark, L.; Teijido, O.; van der Wel, P. C. A.; Garces, R.; Wagner, G.; Rostovtseva, T. K.; Griffin, R. G. Lipid Dynamics and Protein-Lipid Interactions in 2D Crystals Formed with the Beta-Barrel Integral Membrane Protein VDAC1. *J. Am. Chem. Soc.* **2012**, *134*, 6375−87.
(54) Sigworth, F. J.; Sine, S. M. Data Transformations for Improved Display and Fitting of Single-Channel Dwell Time Histograms. *Biophys. J.* **1987**, *52*, 1047−54.
(55) Weinrich, M.; Worcester, D. L.; Bezrukov, S. M. Lipid Nanodomains Change Ion Channel Function. *Nanoscale* **2017**, *9*, 13291−97.
(56) Nystrom, N. A.; Levine, M. J.; Roskies, R. Z.; Scott, J. R. Bridges: A Uniquely Flexible HPC Resource for New Communities and Data Analytics. *Proceedings of the 2015 XSEDE Conference: Scientific Advancements Enabled by Enhanced Cyberinfrastructure*; ACM: St. Louis, MO, 2015; pp 1−8.
(57) Towns, J.; Cockerill, T.; Dahan, M.; Foster, I.; Gaither, K.; Grimshaw, A.; Hazlewood, V.; Lathrop, S.; Lifka, D.; Peterson, G. D.; Roskies, R.; Scott, J. R.; Wilkins-Diehr, N. XSEDE: Accelerating Scientific Discovery. *Comput. Sci. Eng.* **2014**, *16*, 62−74.
(58) Vrugt, J. A.; ter Braak, C. J. F.; Diks, C. G. H.; Robinson, B. A.; Hyman, J. M.; Higdon, D. Accelerating Markov Chain Monte Carlo Simulation by Differential Evolution with Self-Adaptive Randomized Subspace Sampling. *Int. J. Nonlin. Sci. Num.* **2009**, *10*, 273−90.
(59) Kienzle, P. A.; Krycka, J.; Patel, N.; Sahin, I. *Bumps* (version 0.7.5.4) [Computer Software]; University of Maryland: College Park, MD, 2011.

https://dx.doi.org/10.1021/acsnano.0c07672
ACS Nano 2021, 15, 989−1001